



1    **An improved global land cover mapping in 2015 with 30**  
2    **m resolution (GLC-2015) based on a multi-source product**  
3    **fusion approach**

4    Bingjie Li <sup>1</sup>, Xiaocong Xu <sup>1</sup>, Xiaoping Liu <sup>1,2</sup>, Qian Shi <sup>1</sup>, Haoming Zhuang <sup>1</sup>, Yaotong  
5    Cai <sup>1</sup> and Da He <sup>1</sup>

6    <sup>1</sup>School of Geography and Planning, Sun Yat-Sen University, Guangzhou, 510275, China

7    <sup>2</sup>Southern Marine Science and Engineering Guangdong Laboratory (Zhuhai), Zhuhai, 519080, China

8    *Correspondence to:* Xiaoping Liu (liuxp3@mail.sysu.edu.cn)

9    **Abstract.** Global land cover (GLC) information with fine spatial resolution is a fundamental data input  
10   for studies on biogeochemical cycles of the Earth system and global climate change. Although there are  
11   several public GLC products with 30 m resolution, considerable inconsistencies were found among them  
12   especially in fragmented regions and transition zones, which brings great uncertainties to various  
13   application tasks. In this paper, we developed an improved global land cover map in 2015 with 30 m  
14   resolution (GLC-2015) by fusing multiple existing land cover products based on the Dempster-Shafer  
15   theory of evidence (DSET). Firstly, we used more than 160,000 global point-based samples to locally  
16   evaluated the reliability of the input GLC products for each LC class within each 4°×4° geographical  
17   grid for the establishment of the basic probability assignment (BPA) function. Then, the Dempster's rule  
18   of combination was used for each 30 m pixel to derive the combined probability mass of each possible  
19   land cover class from all the candidate maps. Finally, each pixel was determined with a land cover class  
20   based on a decision rule. Through this fusing process, each pixel is expected to be assigned with the land  
21   cover class that contributes to achieve a higher accuracy. We assessed our product separately with 34,987  
22   global point-based samples and 144 global patch-based samples. Results show that, the GLC-2015 map  
23   achieved the highest mapping performance globally, continentally, and eco-regionally compared with the  
24   existing 30 m GLC maps, with an overall accuracy of 76.0% (83.8%) and a kappa coefficient of 0.715  
25   (0.548) against the point-based (patch-based) validation samples. Additionally, we found that the GLC-  
26   2015 map showed substantial outperformance in the areas of inconsistency, with an accuracy



27 improvement of 17.6%-23.2% in areas of moderate inconsistency, and 21.0%-25.2% in areas of high  
28 inconsistency. Hopefully, this improved GLC-2015 product can be applied to reduce uncertainties in the  
29 research on global environmental changes, ecosystem service assessments, and hazard damage  
30 evaluations, etc. The GLC-2015 map developed in this study is available at  
31 <https://doi.org/10.6084/m9.figshare.19752856.v1> (Li et al., 2022).

## 32 **1. Introduction**

33 Land cover (LC), influenced by both nature and human activities (Running, 2008; Gong et al., 2013;  
34 Song et al., 2018; Liu et al., 2021a), is a significant component of the Earth system (Yang and Huang,  
35 2021). Global land cover (GLC) products can serve as fundamental data for various studies, such as  
36 climate and environmental changes (Bounoua et al., 2002; Foley et al., 2005; Grimm et al., 2008; Yang  
37 et al., 2013; Schewe et al., 2019), food security (Verburg et al., 2013; Ban et al., 2015), carbon cycling  
38 (Moody and Woodcock, 1994; Defries et al., 2002; Gómez et al., 2016), biodiversity conservation  
39 (Chapin et al., 2000; Giri et al., 2005) and land management (Mayaux et al., 2004; Verburg et al., 2011).  
40 Therefore, there is a pressing need for detailed, accurate, and high-quality GLC product to support global  
41 change research and sustainable development.

42 In the preliminary stage, LC mapping mainly relied on visual interpretation, which is time-  
43 consuming, labor-intensive and difficult to be applied at the global scale (Gong, 2012). In recent decades,  
44 satellite remote sensing data, which can provide information of large area coverage and long-term  
45 monitoring, has been adopted to generate GLC products. With coarse resolution satellite data such as  
46 Advanced Very High Resolution Radiometer (AVHRR), Moderate Resolution Imaging  
47 Spectroradiometer (MODIS), Medium Resolution Imaging Spectrometer (MERIS), and Global Land  
48 Surface Satellite (GLASS), a variety of GLC products have been developed at 5 km to 300 m  
49 resolution (Loveland et al., 2000; Hansen et al., 2000; Bartholomé and Belward, 2005; Friedl et al., 2010;  
50 Defourny et al., 2018; Liu et al., 2020a). Although these GLC products have been widely applied to many  
51 applications, it has been proved that the differences between sensors, classification systems, and  
52 considerably low accuracies in areas prevent harmonization of these products (Herold et al., 2008;  
53 Verburg et al., 2011; Grekousis et al., 2015). Also, these products are far from providing enough fine  
54 spatial details of LC due to their relatively coarse spatial resolution, which does not meet the demand of



55 many studies (Giri et al., 2013; Yang et al., 2017). To allow researches which can capture most human  
56 activity, finer-resolution (e.g., 30 m) GLC products are demanded (Giri et al., 2013).

57 With the free accessibility of high-resolution satellite remote sensing data, GLC mapping at fine  
58 resolution has been successfully conducted. Using Landsat imagery, there has been a milestone  
59 achievement that the two GLC products are generated with fine resolution of 30 m, namely Finer  
60 Resolution Observation and Monitoring of Global Land Cover product (FROM\_GLC)(Gong et al.,  
61 2013)and Globeland30 (Chen et al., 2015). After that, a 30 m-resolution GLC mapping in 2017 was  
62 achieved using the first all-season sample set (Li et al., 2017). More recently, Zhang et al. (2021) used  
63 both Landsat time series imagery and high-quality training data from the Global Spatial Temporal Spectra  
64 Library (GSPECLib) to produce a 30 m GLC map in 2015 (GLC\_FCS30) with a two-level classification  
65 scheme. Several attempts have been made to improve accuracy of 30 m GLC products which are  
66 prevail in the generation of GLC mapping task over the last few years. FROM\_GLC was created by  
67 employing four classification algorithms to classify the Landsat images and choosing time series of  
68 MODIS EVI data for training and test. Globeland30 was created by proposing a pixel-object-knowledge-  
69 based (POK) method to assure consistency and accuracy. GLC\_FCS30 was generated by adopting local  
70 adaptive random forest models with high-quality training samples derived from GSPECLib.

71 Despite the great efforts in producing more accurate products, the existing 30 m GLC products still  
72 show low accuracy performance in certain LC classes and some specific areas (Sun et al., 2016; Kang et  
73 al., 2020). Furthermore, the existing 30 m products showed great agreement in overall spatial distribution  
74 patterns but significant spatial inconsistency in some specific areas (heterogeneous areas and transition  
75 zones) and spectrally similar classes (forest and shrubland, cropland and grassland) (Gao et al., 2020;  
76 Liu et al., 2021b). The high spatial inconsistency between the existing 30m GLC products are resulted  
77 from differences in their classification systems, classification techniques employed, source data, and  
78 spatial distribution and size of training samples (Yang et al., 2017; Gao et al., 2020). Due to the aforesaid  
79 limitations, users of GLC products still have difficulties in an appropriate selection of data for their  
80 specific application. Ultimately, this situation leads to uncertainties in outcomes of related researches  
81 when different 30 m GLC products are used. For GLC mapping with fine spatial resolution, more efforts  
82 should be focused on improving the mapping in heterogenous and fragmented landscape (Herold et al.,  
83 2008; Liu et al., 2021b). Therefore, it is pressing to generate a more accurate and reliable GLC product



84 with high classification accuracy, especially for spatially inconsistent regions and low-accuracy LC  
85 classes.

86 According to Gong et al. (2016), inconsistencies between LC products indicate available  
87 complementary information and more robust and reliable data can be generated by integrating the input  
88 maps with the data fusion method. Given that different maps have disagreement and provide accurate  
89 information in different locations, we can make a best choice for the class label assigned to each pixel  
90 by weighting the credibility of all the available information and combining them through a decision rule  
91 (Clinton et al., 2015). In this way, the output map of integration on input maps can reduce the overall risk  
92 of assigning a wrong class label to a pixel and at least achieve the average performance of input maps.  
93 Several attempts have been made to employ a data fusion method for producing an accurate and  
94 consistent LC map. Jung et al. (2006) generated a 1km GLC map by combination of MODIS, GLC2000  
95 and GLCC data. Fritz et al. (2011) proposed a synergy method on five existing cropland datasets to map  
96 the cropland extent in Sub-Saharan Africa. See et al. (2015) generated two GLC products by integrating  
97 medium resolution LC products with geographically weighted regression (GWR). Song et al. (2017)  
98 improved forest cover classification at the global scale using a data fusion method based on machine  
99 learning. All of these researches have demonstrated that fusion method can create an integrated LC  
100 product where the mapping accuracy is greatly improved by combing the best of candidate maps.

101 In this research, we propose a multi-source product fusion approach on the Google Earth Engine  
102 (GEE) platform to produce an improved GLC product in 2015 (GLC-2015) with 30 m resolution. The  
103 fusion approach we proposed aims to deal with the inconsistency between previous 30 m GLC products  
104 and generate a map which has better mapping performance than any of the candidate maps by evaluating  
105 the mapping accuracy of these existing products at the local scale and choosing the most credible LC  
106 class. To fulfill the purpose, we first performed reliability evaluation, where the accuracy of each GLC  
107 product for each LC class in each  $4^\circ \times 4^\circ$  geographical grid is regarded as the evidential probability to  
108 create the BPA function. Then, the BPA values of all the LC classes from different GLC products are  
109 fused according to the Dempster's rule of combination. Finally, the GLC-2015 map was integrated after  
110 a final accepted LC class with the maximum combined probability mass was assigned to each 30 m pixel.  
111 Our GLC-2015 map was separately validated with two different validation sets, namely global point-  
112 based samples and global patch-based samples, and compared with three existing multiple-class GLC



113 products. Moreover, we provided an analysis for mapping improvement of the GLC-2015 compared to  
114 other products in areas of high mapping inconsistency. The GLC-2015 map is proved to be accurate and  
115 credible and can significantly improve the mapping accuracy in areas of high inconsistency between  
116 previous products.

## 117 **2. Datasets**

### 118 **2.1 Multiple-class GLC products**

119 Three existing 30m GLC products with multiple classes, including GlobeLand30, FROM\_GLC and  
120 GLC\_FCS30, were employed as input maps in the fusion based on DSET. A summary of their detailed  
121 information is shown in Table 1.

122 GlobeLand30, a widely-used global geo-information product, was produced by the POK-based  
123 method using Landsat and HJ-1 satellite images. Globeland30 products are freely accessible online at  
124 the website (<http://www.globalland30.org>) for 2000 and 2010. From the accuracy assessment, the  
125 Globeland30 for the year 2010 had an overall accuracy exceeded 80% using large samples (Chen et al.,  
126 2015). We employed the version of 2010 as one of the candidate maps for the mapping procedure.

127 FROM\_GLC was first generated using numerous Landsat images, which has a fine classification  
128 system with a two-level structure. It achieved an OA of 64.5% through validation with the complete test  
129 samples and 71.5% with a subset of test samples in homogeneous areas (Gong et al., 2013). We used the  
130 version of 2015 for the fusion.

131 GLC\_FCS30 was developed using Landsat time series data and large training samples from the  
132 GSPECLib. It has a two-level classification scheme that contains 16 global LCCS LC classes and 14  
133 detailed regional LC classes. The overall accuracy of the GLC\_FCS30 according to LCCS level-1  
134 validation scheme reached 71.4% (Zhang et al., 2021).



135 **Table 1. Detailed information of GLC products used in this paper.**

Product name	Satellite sensors	Year of reference	Access	Literature
Globeland30	Landsat TM/ETM+	2010	<a href="http://www.globallandcover.com/">http://www.globallandcover.com/</a>	(Chen et al., 2015)
	HJ-1 A/B			
FROM_GLC	Landsat TM/ETM+/OLI	2015	<a href="http://data.ess.tsinghua.edu.cn/">http://data.ess.tsinghua.edu.cn/</a>	(Gong et al., 2013)
GLC_FCS30	Landsat OLI	2015	<a href="https://doi.org/10.5281/zenodo.3986872">https://doi.org/10.5281/zenodo.3986872</a>	(Zhang et al., 2021)
GAUD	Landsat TM/ETM+/OLI	2015	<a href="https://doi.org/10.6084/m9.figshare.11513178.v1">https://doi.org/10.6084/m9.figshare.11513178.v1</a>	(Liu et al., 2020b)
GFC	Landsat TM/ETM+	2015	<a href="http://earthenginepartners.appspot.com/science-2013-global-forest">http://earthenginepartners.appspot.com/science-2013-global-forest</a>	(Hansen et al., 2013)
JRC GSW	Landsat TM/ETM+/OLI	2015	<a href="http://global-surface-water.appspot.com/">http://global-surface-water.appspot.com/</a>	(Pekel et al., 2016)
GMW	ALOS PALSAR	2015	<a href="https://data.unep-wcmc.org/datasets/45">https://data.unep-wcmc.org/datasets/45</a>	(Bunting et al., 2018)
	Landsat TM/ETM+			

136 **2.2 Single-class GLC products**

137 To improve the quality of the fusing result, a set of highly qualified GLC products with single class at 30  
 138 m fine resolution were also used. Compared to the multiple-class GLC products, these single-class GLC  
 139 products are more likely to provide accurate information since they usually focus on promoting mapping  
 140 performance of specific LC class. These products include Global Forest Change (GFC) (Hansen et al.,  
 141 2013), Global Annual Urban Dynamics (GAUD) (Liu et al., 2020b), Joint Research Centre's Global  
 142 Surface Water (JRC GSW) (Pekel et al., 2016), and Global Mangrove Watch (GMW) (Bunting et al.,  
 143 2018). While these single-class products are either annual or multi-epoch, we only selected these  
 144 products in the target year of 2015. Table 1 also describes the information of these selected single-class  
 145 GLC products.

146 GFC was resulted from a time-series analysis of growing season Landsat scenes, aiming to provide  
 147 information about global tree cover extent, gain, and loss at a 30m spatial resolution. The accuracy  
 148 assessment was performed at global and climate domain scales and the forest gain reached an overall  
 149 accuracy of 99.6% and forest loss reached 99.7% across the globe (Hansen et al., 2013). Up to now, it  
 150 has a temporary coverage from 2000 to 2020.

151 GAUD, which provides 30m annual urban extent for the time period of 1985 to 2015, was generated  
 152 using numerous Landsat images with both data fusion approach and temporal segmentation approach on



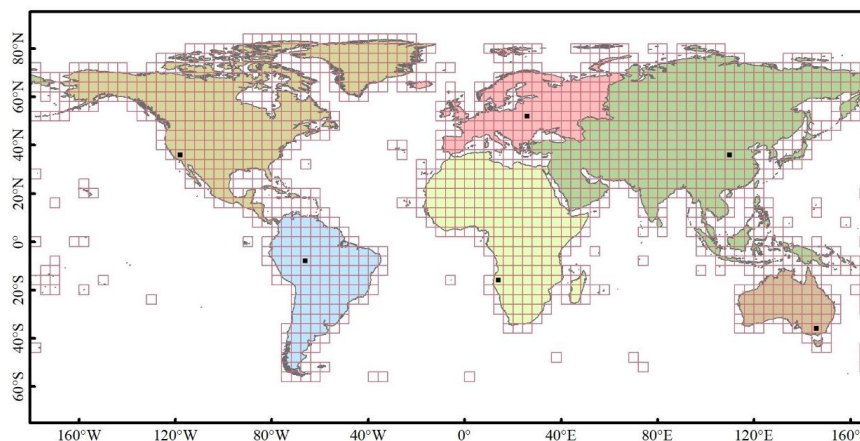
153 the GEE platform. Validation was conducted across different urban ecoregions and the globe by the  
154 product developer. The accuracies of mapping urbanized year are 76% for the period of 1985 to 2000  
155 and 82% for the period of 2000 to 2015 at humid regions worldwide (Liu et al., 2020b).

156 JRC GSW dataset provides a monthly presentation of global surface water changes from 1984 to  
157 2015 at a fine 30 m resolution. Expert systems, visual analytics and evidential reasoning were exploited  
158 to detect water extent and changes. Based on 40,124 validation points over the globe and across the 32  
159 years, commission accuracies were determined with overall accuracies of 99.45% (TM), 99.35% (ETM+)  
160 and 99.54% (OLI) and omission accuracies were reflected in overall accuracies of 97.01% (TM), 95.79%  
161 (ETM+) and 96.25%(OLI) (Pekel et al., 2016). The product is now updated to 2020 on the GEE platform.

162 GMW dataset was produced as a resulted of the GMW initiative, which aims to provide consistent  
163 information of mangrove extent. The global mangrove map in 2010 was generated as a baseline map  
164 employing the Extremely Randomized Trees classifier to classify ALOS PALSAR and Landsat imagery.  
165 Assessed by a total of 53,878 sample points globally, the overall accuracy of the baseline map reached  
166 95.3% and the producer's accuracy achieved 94.0% (Bunting et al., 2018). Based on the baseline in 2010,  
167 mangrove extent maps for six epochs between 1996 and 2016 have been established and annual change  
168 monitoring from 2018 and onwards are undertaken.

### 169 **2.3 Global point-based and patch-based samples**

170 In this study, we collected two sets of global samples, namely the global point-based samples and the  
171 global patch-based samples. To collect representative and sufficient samples efficiently, we divided the  
172 world's terrestrial area into  $4^{\circ} \times 4^{\circ}$  geographical grids. A total of 1,507 grids are distributed evenly across  
173 the globe, shown as Fig. 1.

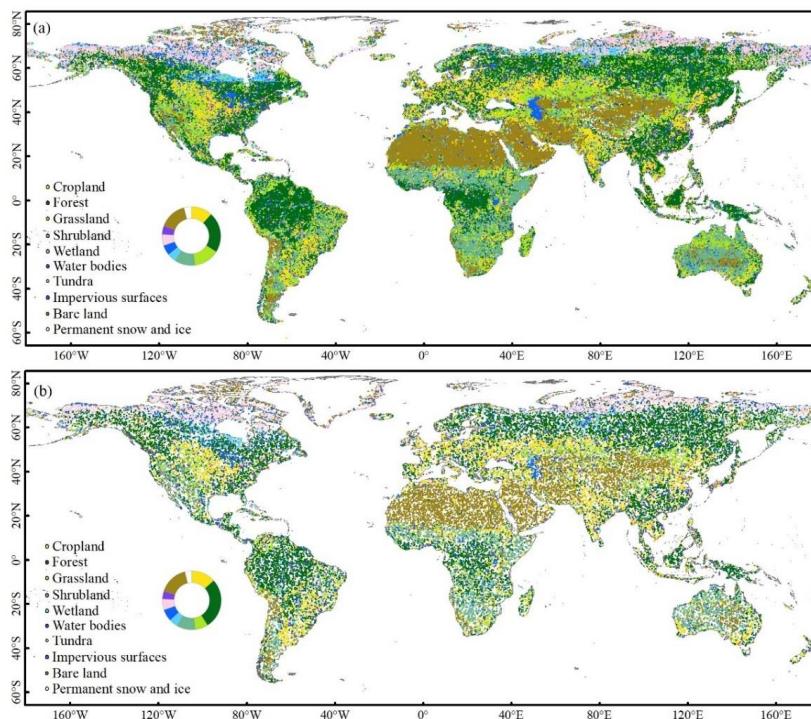


174

175 **Figure 1. Spatial distribution of the  $4^\circ \times 4^\circ$  geographical grids over the world. Six black rectangle tiles with**  
176 **size of  $0.25^\circ$  were used for visual comparison between our product and other three products.**

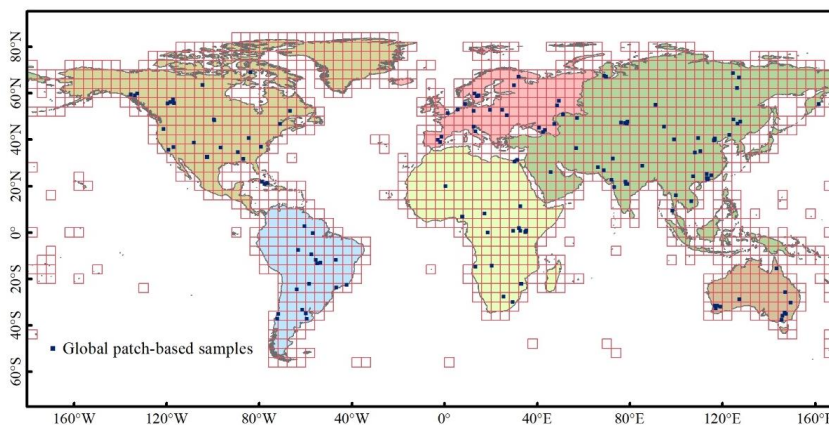
177 In order to derive the global point-based samples, we adopted stratified random sampling in each  
178 grid. First, the FROM\_GLC product was used to calculate the area ratio of each LC class. Then, points  
179 were randomly extracted with the LC class label taken from the FROM\_GLC according to the area ratio  
180 and spatial location of each class. Finally, more than 20,000 global samples were collected. Through the  
181 sampling method mentioned above, the global point-based samples were even across the globe and  
182 sufficient for each LC class in each grid. Therefore, more than 50 points could be easily derived for LC  
183 classes with a small area ratio in the  $4^\circ \times 4^\circ$  grid. Since the FROM\_GLC shows low accuracy for some  
184 LC classes, especially for cropland and forest (Gao et al., 2020; Liu et al., 2021b; Zhang et al., 2021;  
185 Zhang et al., 2022), there were inevitably errors in the selected global samples. To guarantee that the  
186 samples are accurate, all the points were checked visually according to Google Earth high-resolution  
187 images and rectified if they were wrongly labeled. The whole sample set was randomly split into two  
188 subsets: 80% of the global samples were used to assess the accuracy of each GLC product for various  
189 LC classes at the global scale and in each grid. The remaining 20% were used for the validation of the  
190 GLC-2015 map and data inter-comparison between different GLC products. Figure 2 presents the  
191 distribution of the whole global point-based samples and the subset for accuracy assessment and data  
192 inter-comparison.





193  
194 **Figure 2. Spatial distribution of (a) the global point-based samples, (b) the subset of the global point-based**  
195 **samples for accuracy assessment and data inter-comparison, the proportions of each LC class are shown in**  
196 **the pie chart.**

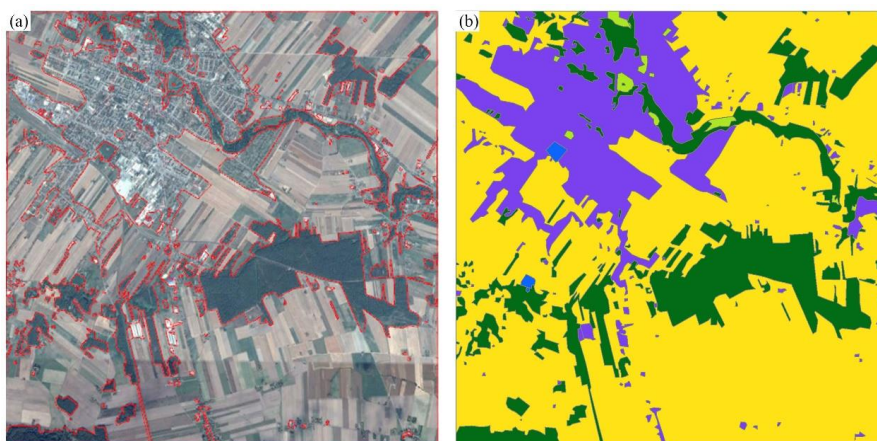
197 To verify the consistency between the GLC-2015 and the actual pattern of the landscape at the local  
198 scale, we also established the global patch-based samples. First, we randomly selected 93 grids of  $4^\circ \times$   
199  $4^\circ$  from a total of 1,507 grids worldwide. Secondly, each selected grid was divided into  $5 \text{ km} \times 5 \text{ km}$   
200 blocks, and we randomly collected one to five blocks from each grid. In total, there were 144 blocks  
201 selected as the global patch-based samples, as displayed in Fig. 3. Finally, for each block in the patch-  
202 based samples, we used ArcGIS 10.5 software to derive polygons (patches) of various sizes which  
203 captured the real landscape on the Sentinel-2 images. Meanwhile, each polygon was manually labeled  
204 with a LC class. An example of producing a patch-based sample is shown in Fig. 4.



205

206

**Figure 3. Spatial distribution of the global patch-based samples.**



207

208

209

210

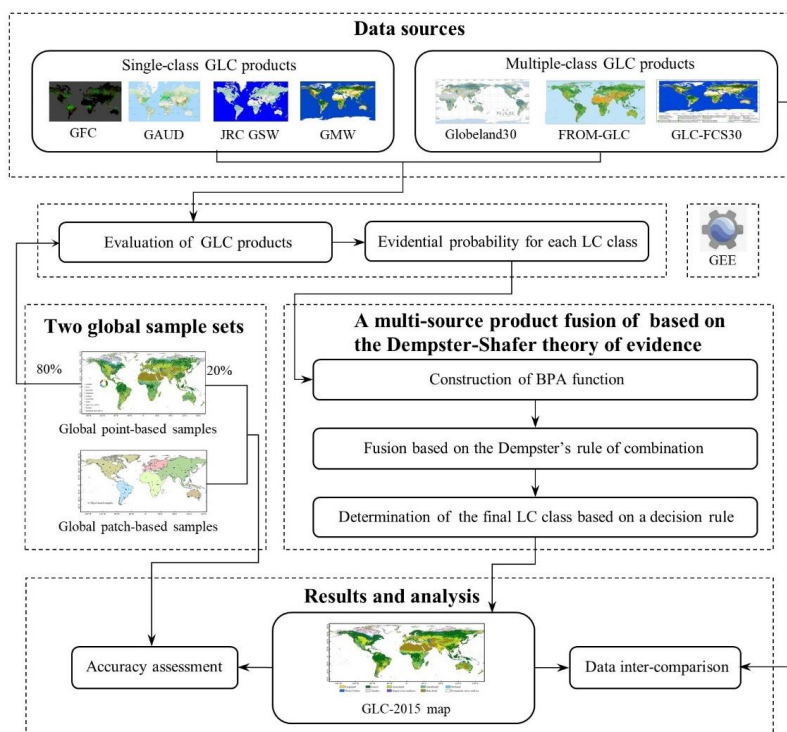
**Figure 4. An example of the production of global patch-based samples based on manual interpretation. The results after vectorization of a Sentinel-2 image are shown as (a) and the corresponding patch-based sample is shown as (b).**

### 211 3. Methods

212 In this study, we proposed a multi-source product fusion method to produce the GLC-2015 map. The  
213 procedure mainly comprised the fusion based on the Dempster-Shafer theory of evidence (DSET),  
214 accuracy assessment and data inter-comparison (Fig. 5). The basic of this study is the fusion of multi-  
215 source GLC products based on DSET. The fusion method was performed at the pixel level and it involves  
216 the following three main steps: (1) Construct the basic probability assignment (BPA) function of each  
217 pixel that belongs to each LC class considering the accuracy assessment of different GLC products; (2)



218 calculate the combined probability mass for each class per pixel using the Dempster's rule of combination;  
219 and (3) determine the finally accepted LC class per pixel by a decision rule. Afterwards, pixels with a  
220 determined LC class were integrated to generate a new map. To improve mapping and analysis efficiency,  
221 the entire framework was implemented in all  $4^\circ \times 4^\circ$  geographical grids on the GEE platform.



222  
223 **Figure 5. The framework for generating the GLC-2015 map using a multi-source product fusion approach**  
224 **based on DEST.**

### 225 3.1 Definition of the classification system

226 Due to the applications for different social needs, the existing GLC products were produced with different  
227 classification systems (Table S1). The GlobeLand30 used a simple classification system that only  
228 contained 10 first-level classes. Unlike the GlobeLand30, the FROM\_GLC and GLC\_FCS30 were  
229 classified with a two-level classification scheme. Through analysis of these systems, we found that the  
230 classification systems are not the same, but they have some agreements. For example, there are both 10  
231 major classes which have the same definition in the GlobeLand30 and FROM\_GLC. Additionally, in  
232 contrast to the GlobeLand30 and FROM\_GLC, the level-0 classification system of the GLC\_FCS30



233 lacks tundra. However, in the level-2 detailed LC classes of the GLC\_FCS30, Lichens/mosses has little  
234 distinction with tundra. Separately, we selected Lichens/mosses and renamed it as tundra, one of the first-  
235 level classes. In this study, we adopted the classification system with 10 LC classes, including cropland,  
236 forest, grassland, shrubland, wetland, water bodies, tundra, impervious surfaces, bare land, and  
237 permanent snow and ice (Chen et al., 2015), as listed in Table 2. With the discrepancy in the classification  
238 system taken into consideration, the 30 level-2 detailed LC classes of GLC\_FCS30 were reclassified into  
239 10 major classes according to the classification scheme adopted by our mapping process.

240 **Table 2. Classification system adopted in this paper.**

Id	LC class	Definition
10	Cropland	Land areas used for food production and animal feed.
20	Forest	Land areas dominated by trees with tree canopy cover over 30%.
30	Grassland	Land areas dominated by natural grass with a cover over 10%.
40	Shrubland	Land areas dominated by shrubs with a cover over 30%.
50	Wetland	Land areas dominated by wetland plants and water bodies.
60	Water bodies	Land areas covered with accumulated liquid water.
70	Tundra	Land areas dominated by lichen, moss, hardly perennial herb and shrubs in the polar regions.
80	Impervious surfaces	Land areas covered with artificial structures.
90	Bare land	Land areas with scarce vegetation with a cover lower than 10%.
100	Permanent snow and ice	Land areas dominated by permanent snow, glacier and icecap.

### 241 3.2 A multi-source product fusion for the GLC-2015 mapping

242 The DSET is an effective method widely applied for the fusion of multi-source data. To generate a new  
243 high-quality GLC map, a multi-source product fusion method using DSET was proposed. In the  
244 remainder of the section 3.2, We introduced the overview on the theory and presented the application of  
245 DSET in our mapping process.

#### 246 3.2.1 Dempster-Shafer theory of evidence

247 The DSET is developed by Dempster and Shafer, which is an extension of Bayesian probability theory.  
248 This theory treats information from different data sources as independent evidence and integrated these  
249 evidences with no requirements regarding the prior knowledge. In the fusion, we assume a classification



250 process in which all the input data are to be classified into mutually exclusive classes. Let the set  $\Omega$  of  
 251 these classes be a frame of discrimination.  $2^\Omega$  is the power set of  $\Omega$  that includes all the classes and  
 252 their possible unions. We defined the function  $m: 2^\Omega \rightarrow [0,1]$  as the basic probability assignment (BPA)  
 253 function if and only if it satisfies  $m(\Phi) = 0$  and  $\sum_{A \subseteq 2^\Omega} m(A) = 1$  with  $\emptyset$  denotes an empty set. For  
 254 each class  $A \subseteq 2^\Omega$ ,  $m(A)$  is called the basic probability mass which can be computed from the BPA  
 255 function and represents the degree of support for class A or confidence in class A.

256 The purpose of fusion is to evaluate and integrate information from multiple sources. In the DSET,  
 257 these multi-source data are regarded as different evidence and provide different assessments. To generate  
 258 all the evidences, Dempster-Shafer theory of evidence offers a rule. Suppose  $m_i(B_j)$  is the basic  
 259 probability mass computed from the BPA function for each input data  $i$  with  $1 \leq i \leq n$  for all classes  
 260  $B_j \in 2^\Omega$ . Dempster's rule of combination is provided to calculate a combined probability mass from  
 261 different evidences. The fusion rules are given in equation (1) and (2).

$$262 \quad m(C) = \frac{\sum_{B_1 \cap B_2 \dots \cap B_n = C} \prod_{1 \leq i \leq n} m_i(B_j)}{1 - k} \quad (1)$$

263

$$264 \quad k = \sum_{B_1 \cap B_2 \dots \cap B_n = \emptyset} \prod_{1 \leq i \leq n} m_i(B_j) \quad (2)$$

265 Where  $k$  represents the basic probability mass associated with conflicts among the sources of evidence.  
 266  $C$  is the intersection of all classes  $B_j$  and carries the joint information from all the input data. After the  
 267 combination, we took a decision rule to decide the class we finally accept. There are several ways to  
 268 decide the final class by simply choosing the class with the maximum belief, plausibility, support, or  
 269 commonality.

### 270 3.2.2 Mapping based on DSET

271 Here, we presented our implementation for the GLC-2015 mapping in the framework of DSET. All the  
 272 multiple-class and single-class GLC products described in Sect. 2 were selected as input maps to be  
 273 combined. In the integration of multi-source GLC products, since all the LC classes in our classification  
 274 system are known, the frame of discrimination was defined to be our classification system:

$$275 \quad \Omega = \left\{ \begin{array}{l} \text{cropland, forest, grassland, shrubland, wetland, water bodies,} \\ \text{tundra, impervious surfaces, bare land, permanent snow and ice} \end{array} \right\} \quad (3)$$

276 The definition of BPA function is the critical point in applying DSET (Rottensteiner et al., 2005).  
 277 In the fusion, we wanted to achieve a per-pixel classification into one of ten LC classes: cropland, forest,



278 grassland, shrubland, wetland, water bodies, tundra, impervious surfaces, bare land, and permanent snow  
 279 and ice. For each single-class or multiple-class GLC product, the accuracy for each LC class was  
 280 calculated and used as evidential probability to construct the BPA. Here, we defined the BPA function as  
 281 follow:

$$282 \quad m_i(T_j) = \frac{PA_{local(ij)} + UA_{local(ij)}}{2} \times 75\% + \frac{PA_{global(ij)} + UA_{global(ij)}}{2} \times 25\% \quad (4)$$

283 Where  $m_i(T_j)$  represents the BPA function of evidence source  $i$  for the LC class  $T_j$ ;  $PA_{local(ij)}$ ,  
 284  $UA_{local(ij)}$  denote producer's accuracy and user's accuracy of evidence source  $i$  for the LC class  $T_j$  for  
 285 each  $4^\circ \times 4^\circ$  geographical grid, respectively;  $PA_{global(ij)}$ ,  $UA_{global(ij)}$  denote producer's accuracy and  
 286 user's accuracy of evidence source  $i$  for LC class  $T_j$  at the global scale.

287 To estimate the exact values of  $PA_{local(ij)}$ ,  $UA_{local(ij)}$ ,  $PA_{global(ij)}$  and  $UA_{global(ij)}$ , we used 80%  
 288 of the global point-based samples more than 160,000 points derived in Sect 2.3. As soon as we obtained  
 289 the measurements of  $m_i(T_j)$ , the combined probability masses  $m(T_j)$  were evaluated based on  
 290 Dempster's rule of combination for each pixel classified as the LC class  $T_j$  by fusing BPA values of all  
 291 the evidence sources:

292

$$293 \quad m(T_j) = \frac{1}{1-k} \sum_{T_{1j} \cap T_{2j} \dots \cap T_{nj} = T_j} m_i(T_j) \quad (5)$$

294

$$295 \quad k = \sum_{T_{1j} \cap T_{2j} \dots \cap T_{nj} = \emptyset} m_i(T_j) \quad (6)$$

296 Where  $k$  represents the basic probability mass associated with conflict;  $m_i(T_j)$  represents the basic  
 297 probability mass of a certain pixel belonging to the LC class  $T_j$  from different GLC products.

298 Additionally, a belief measure (Bel) was given to measure the degree of credibility that a pixel  
 299 labeled as the finally accepted LC class when combining all the available evidences. The belief measure  
 300 was determined by

$$301 \quad Bel(T_j) = \sum_{T_{ij} \in T_j} m_i(T_j) \quad (7)$$

302 To determine the finally accepted LC class per pixel, we took the rule of maximum combined  
 303 probability mass as our decision rule and the LC class with the maximum combined probability mass is  
 304 assigned to the 30 m pixel. Pixels labeled with the LC class were integrated to generate the GLC-2015



305 product.

### 306 3.3 Accuracy assessment

307 To assess the accuracy of the GLC-2015 map, we utilized two validation methods: validation with the  
308 global point-based samples and the global patch-based samples. Since the global point-based sample set  
309 is distributed evenly across the world and its sample size for each LC class is relatively sufficient and  
310 balanced, even for the rare classes, it can provide a representative and credible basis for estimation of the  
311 GLC-2015 map globally. Furthermore, we used the global patch-based samples to conduct accuracy  
312 assessment from the local landscape scale. Although the global patch-based sample set provide an  
313 inadequate sample size for rare LC classes, it can take advantage of the spatial context information and  
314 efficiently reflect the actual pattern of the landscape.

315 The error matrix was produced to evaluate and analyze the GLC-2015 mapping result. The error  
316 matrix is composed of entry  $A_{ij}$ , which represents the number of samples with reference LC class  $j$   
317 being classified as LC class  $i$ . The overall accuracy (OA), kappa coefficient, producer's accuracy (PA),  
318 and user's accuracy (UA) were generated from error matrix to describe the quality of the GLC-2015 map.  
319 They are defined as follows:

$$320 \quad OA = \frac{\sum_i A_{ii}}{\sum_i \sum_j A_{ij}} \quad (8)$$

$$321 \quad P_o = OA \quad (9)$$

$$322 \quad P_e = \sum_k \frac{\sum_i A_{ik}}{\sum_i \sum_j A_{ij}} \times \frac{\sum_j A_{kj}}{\sum_i \sum_j A_{ij}} \quad (10)$$

$$323 \quad kappa = \frac{P_o - P_e}{1 - P_e} \quad (11)$$

$$324 \quad PA^i = \frac{A_{ii}}{\sum_k A_{ki}} \quad (12)$$

$$325 \quad UA^i = \frac{A_{ii}}{\sum_k A_{ik}} \quad (13)$$

326 Where  $UA^i$  and  $PA^i$  represent UA and PA of the LC  $i$ , respectively;  $P_o$  is the agreement between the  
327 reference and the classified data;  $P_e$  is the hypothetical probability of chance agreement.

### 328 3.4 Data inter-comparison

329 To better reflect the quality of the GLC-2015 map, we intercompared the GLC-2015 map with the  
330 GlobeLand30, FROM\_GLC and GLC\_FCS30. In the accuracy assessment of different products, two



331 global validation sets described earlier were employed.

332 To figure out whether the GLC-2015 map promotes accuracy in the areas with high classification  
333 difficulty and how much the improvement is compared to the other products, we conducted the spatial  
334 consistency analysis between the GlobeLand30, FROM\_GLC, and GLC\_FCS30 and compared the  
335 mapping performance of the GLC-2015 with others in the areas of low inconsistency, moderate  
336 inconsistency, and high inconsistency. To visually present the spatial consistency between three existing  
337 GLC maps, we employed the spatial superposition method to obtain the spatial correspondence pixel-  
338 by-pixel between different maps. Based on the times of all the GLC products agreed for the same LC  
339 class, the degree of consistency for a pixel was identified as three levels with the agreement value equal  
340 to 3, 2, or 1. The areas of low inconsistency were regarded as pixels that classified as the same LC class  
341 in all three GLC maps (labeled as 3). The moderate inconsistency areas were regarded as pixels that were  
342 consistent in only two GLC maps (labeled as 2). The high inconsistency areas were regarded as pixels  
343 that were totally inconsistent in these three GLC maps (labeled as 1). For a visual comparison, all these  
344 GLC maps were aggregated to  $0.05^\circ$ , in which the LC class with the largest proportion determined the  
345 class in each  $0.05^\circ$  grid.

#### 346 **4. Results and discussion**

##### 347 **4.1 Mapping result of the GLC-2015 map**

348 Using a multi-source product fusion method based on the DSET, we generated an improved 30m global  
349 land cover map in 2015 (GLC-2015). Figure 6 illustrates the GLC-2015 map. The GLC-2015 map can  
350 accurately describe the spatial distribution of various LC classes. For example, cropland areas are mostly  
351 located in Central America, the region from the Hungarian plain to the Siberian plain, the eastern and  
352 southern parts of China, and the most of India. In addition, forest, which is one of the easily  
353 distinguishable classes from the map, is concentrated in the eastern part of North America, the Amazon  
354 basin of South America, the northern part of Eurasia and the equatorial region of Africa.



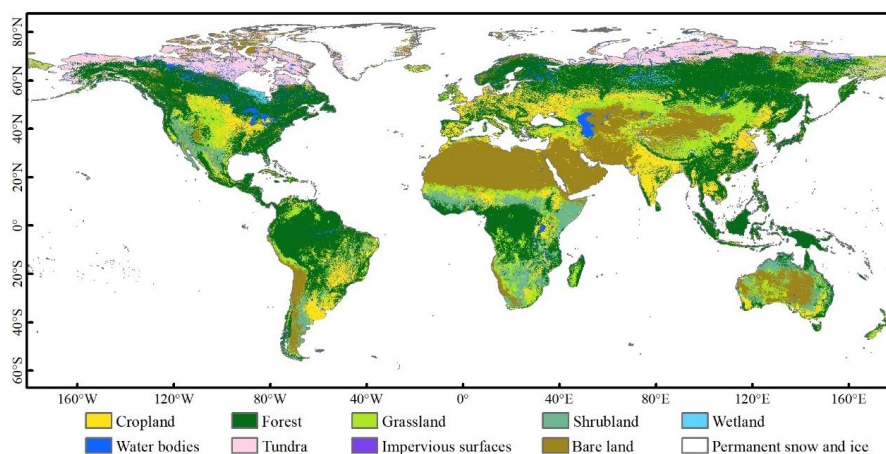


**Figure 6. Global land cover map in 2015 with 30 m resolution (GLC-2015).**

## 357 4.2 Accuracy assessment of the GLC-2015 map

### 358 4.2.1 Accuracy assessment with the global point-based samples

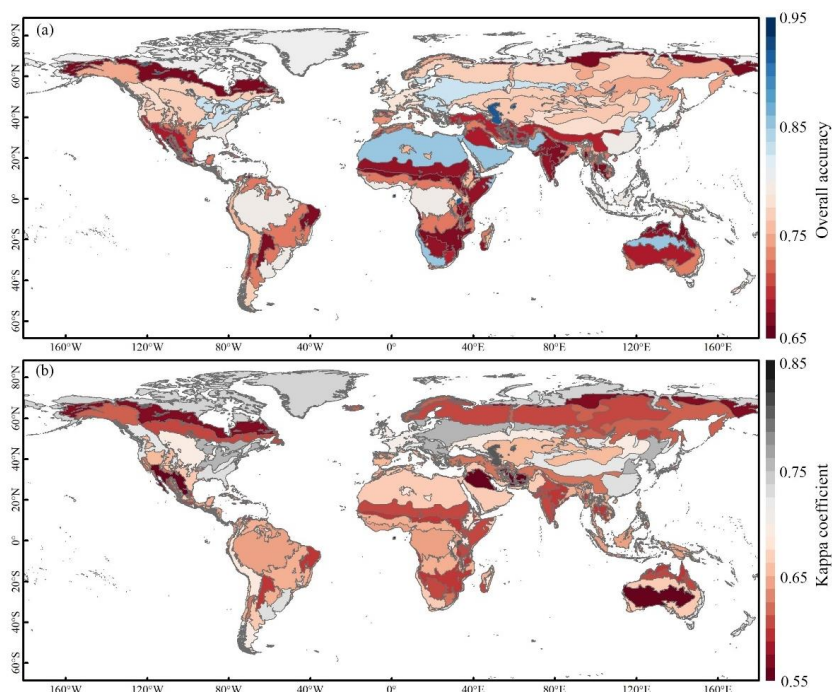
359 The accuracy of the GLC-2015 map was first tested via the global point-based samples, and the results  
360 of assessment are listed in Table 3. The GLC-2015 map achieved an OA of 76.0% and kappa coefficient  
361 of 0.715 at the global scale, demonstrating the good performance of our map. Among all the LC classes,  
362 permanent snow and ice possessed the best mapping performance, with PA and UA achieving 88.1% and  
363 93.2%. The accuracy of water bodies was also high, where PA and UA exceeded 80%. The producer's  
364 accuracy of forest reached 91.7%, while the user's accuracy of that was 78.3%. Grassland, shrubland,  
365 and wetland had relatively low accuracy, with PA below 70%. Among them, grassland and shrubland  
366 were mainly confused with forest, which might be because these classes are both vegetation, thus causing  
367 difficulty in recognition by spectral information. Due to the complex spectral characteristics, wetland is  
368 often mixed with vegetation and water bodies (Ludwig et al., 2019). As shown in the confusion matrix,  
369 49.53% of wetland was misclassified as vegetation and water bodies.



370 **Table 3. The error metric for the GLC-2015 map based on the global point-based samples.**

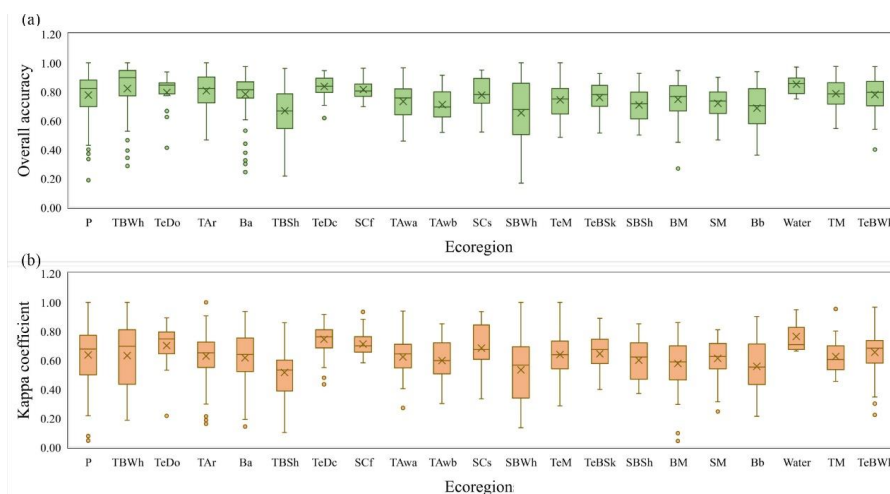
	Cropland	Forest	Grassland	Shrubland	Wetland	Water bodies	Tundra	Impervious surfaces	Bare land	Permanent snow and ice	Total	PA
Cropland	3449	465	418	73	21	53	4	73	96	0	4652	0.741
Forest	173	8888	207	162	92	18	46	46	56	4	9692	0.917
Grassland	65	370	1632	86	29	11	46	41	189	10	2479	0.658
Shrubland	183	539	846	1305	43	32	76	99	514	4	3641	0.358
Wetland	23	587	103	25	659	102	26	14	110	4	1653	0.399
Water bodies	29	107	20	1	86	1937	18	12	51	3	2264	0.856
Tundra	1	269	123	7	0	19	1417	2	268	19	2125	0.667
Impervious surfaces	79	47	13	0	2	15	1	1284	56	1	1498	0.857
Bare land	35	71	330	54	43	104	57	74	4855	40	5663	0.857
Permanent snow and ice	0	11	16	0	4	19	13	1	93	1163	1320	0.881
Total	4073	113543	3708	1713	979	2310	1704	1646	6288	1248	34987	
OA	0.854	0.783	0.440	0.762	0.673	0.839	0.832	0.780	0.772	0.932		
Kappa						0.760						
						0.715						

371 The regional accuracies are presented in Fig. 7. The OA of the GLC-2015 ranged from 66.1% to  
 372 92.7%, and kappa coefficient from 0.552 to 0.813. From the perspective of OA, Water regions lead,  
 373 followed by Tropical desert, Temperate continental forest, and Polar. These are areas with homogeneous  
 374 land cover and have low difficulty in mapping. Tropical desert also achieved high OA, but its kappa  
 375 coefficient was low. Boreal tundra woodland, Tropical dry forest, Tropical shrubland, and Subtropical  
 376 desert are the regions with low OA. The first one may be related to the high latitudes. The followed two  
 377 may be because they belong to areas with complicated and mixed LC classes which is not easily classified.  
 378 The last one may be the consequence of sparse vegetation in desert areas. For the kappa coefficient, the  
 379 ranking was similar to those for OA, expect for that Tropical desert achieved a low kappa coefficient.



380  
381 **Figure 7. Regional accuracy of the GLC-2015 map according to ecoregions. (a)overall accuracy, (b) kappa**  
382 **coefficient. The ecoregion boundaries are obtained from the Food and Agriculture Organization of the United**  
383 **Nations (FAO).**

384 Figure 8 shows the accuracies of the GLC-2015 map in different ecoregions, where Fig. 8a shows  
385 the results of overall accuracy and Fig. 8b of the kappa coefficient. Overall, the mean OA and kappa  
386 coefficient were over 60% and 0.50, respectively. However, the OA ranged from 18.8% to 100% and  
387 kappa coefficient from 0.15 to 1.00, indicating that the accuracies of mapping fluctuated obviously  
388 among different areas. Temperate continental forest and Water regions are the areas with high and stable  
389 accuracies. Subtropical desert is the area where accuracies had relatively large fluctuation.



390

391 **Figure 8. The box-plot of the accuracy for twenty-one ecoregion zones (a) overall accuracy, (b) kappa**  
392 **coefficient. Ecoregion abbreviation and corresponding ecoregion is described in Table S2.**

#### 393 4.2.2 Accuracy assessment with the global patch-based samples

394 The accuracy assessment of the GLC-2015 map was also conducted with the global patch-based samples.

395 Table 4 summarizes the results for accuracy assessment of each LC class in the GLC-2015 map. From

396 the assessment results, it can be found that the OA of the GLC-2015 map reached 83.8%, which was

397 higher than 76.0% tested with the global point-based samples. The kappa coefficient of the GLC-2015

398 map was 0.548, which was 0.167 lower than the result calculated with the global point-based samples.

399 In both accuracy assessment results based on two different validation data sets, water bodies, forest, and

400 permanent snow and ice were validated to have high accuracy, and grassland, shrubland, and wetland

401 were validated to have low accuracy. Nevertheless, the ranking of accuracy for each LC class had a slight

402 difference. For example, in assessment based on the global point-based samples, impervious surfaces

403 and permanent snow and ice ranked higher than that based on the global patch-based samples. This may

404 be because a LC map can easily show where one LC class is distributed but hardly describe its actual

405 shape. In addition to the accuracy assessment on a pixel scale, validation on a patch scale is equally

406 important because it can reflect the shape consistency between the GLC-2015 map and the actual

407 landscape, even if the size of global patch-based samples is relatively small. Overall, no matter from the

408 respective of the global point-based samples or the global patch-based samples, the mapping accuracies

409 of the GLC-2015 map are satisfactory.



410 **Table 4. Mapping accuracy via global patch-based samples for the GLC-2015 map**

	Cropland	Forest	Grassland	shrubland	Wetland	Water bodies	Tundra	Impervious surfaces	Bare land	Permanent snow and ice
PA	0.862	0.899	0.622	0.565	0.234	0.944	0.683	0.740	0.747	0.820
UA	0.918	0.811	0.633	0.673	0.647	0.916	0.881	0.719	0.604	0.750
OA							0.838			
Kappa							0.548			

411 **4.3 Inter-comparison with other GLC products**

412 **4.3.1 Inter-comparison based on the global point-based samples**

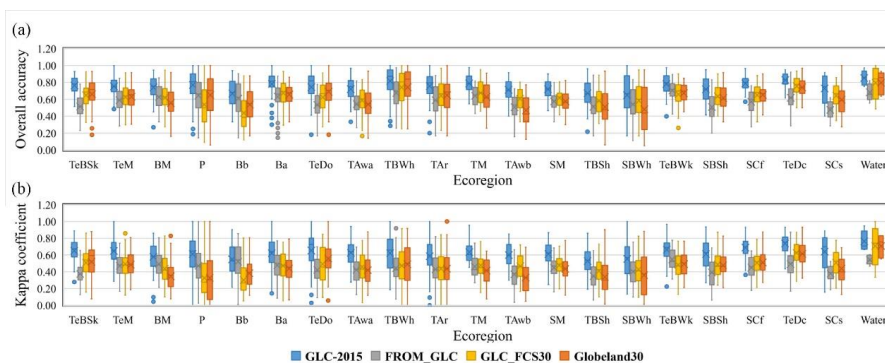
413 Based on the global point-based samples, the inter-comparison of the GLC-2015 map with the  
 414 GlobeLand30, FROM\_GLC, and GLC\_FCS30 were conducted. Since the three products used different  
 415 classification systems, LC classes were transformed to the classification system we adopted in this paper  
 416 to achieve consistent accuracy assessment. The accuracy assessment results for all GLC maps are listed  
 417 in Table 5. It can be found that the GLC-2015 map achieved the highest OA of 76.0% compared with  
 418 GlobeLand30 of 63.5%, FROM\_GLC of 61.3%, and GLC\_FCS30 of 63.5%, respectively. The accuracy  
 419 gap between the GLC-2015 map and other existing ones was 12.5%-14.7%. Also, the GLC-2015 map  
 420 possessed a better kappa coefficient than other products. For each LC class, the GLC-2015 map  
 421 outperformed the other three maps in terms of PA in forest, water bodies, impervious surfaces, bare land,  
 422 and permanent snow and ice. For cropland, grassland, shrub, wetland, and tundra, the GLC-2015 map  
 423 also exhibited better performance for UA than the GlobeLand30, FROM\_GLC and GLC\_FCS30. Overall,  
 424 for the PA or UA, the GLC-2015 map ranked first or second in nearly all LC classes, which demonstrated  
 425 that the GLC-2015 map had smaller omission and commission errors against the other three products.



426 **Table 5. Mapping accuracy of the GLC products with the global point-based samples.**

		Cropland	Forest	Grassland	Shrubland	Wetland	Water bodies	Tundra	Impervious	Bare land	Permanent	OA
									surfaces		snow and ice	(Kappa coefficient)
GLC-2015	PA	0.741	0.917	0.658	0.358	0.399	0.856	0.667	0.857	0.857	0.881	0.760
	UA	0.854	0.783	0.440	0.762	0.673	0.839	0.832	0.780	0.772	0.932	(0.715)
Globeland30	PA	0.749	0.712	0.651	0.208	0.508	0.681	0.770	0.681	0.591	0.806	0.635
	UA	0.770	0.805	0.220	0.386	0.521	0.870	0.575	0.790	0.864	0.907	(0.576)
FROM_GLC	PA	0.385	0.694	0.705	0.389	0.347	0.592	0.705	0.751	0.723	0.875	0.613
	UA	0.647	0.862	0.269	0.418	0.282	0.753	0.687	0.646	0.774	0.763	(0.554)
GLC_FCS30	PA	0.744	0.764	0.389	0.354	0.439	0.600	0.227	0.777	0.783	0.712	0.635
	UA	0.596	0.798	0.314	0.385	0.471	0.804	0.688	0.758	0.637	0.948	(0.568)

427 Further quantitative accuracy assessments of different GLC products were performed in  $4^\circ \times 4^\circ$   
 428 grids using the global point-based samples, and box plots were produced for each product for all grids  
 429 within different ecoregions, as shown in Fig. 9. It can be found that the GLC-2015 map outperformed  
 430 other existing products with the best OA and kappa coefficient across different ecoregions. Also, the  
 431 mean overall accuracy of the GLC-2015 map exceeded 65.0% in all ecoregions, showing the high quality  
 432 of our mapping result. It is worth noting that the GLC-2015 map showed shorter boxes except in  
 433 Subtropical mountain systems, Subtropical desert, Subtropical dry forest, Tropical shrubland, and  
 434 Temperate desert, which means the GLC-2015 map had relatively small fluctuation than other ones. In  
 435 Tropical dry forest, Tropical shrubland, Subtropical desert, and Boreal tundra woodland, the OA and  
 436 kappa coefficient of the four products were relatively low. However, the GLC-2015 map exceeded the  
 437 highest of others by 3.0%-12.9% and greatly improved the mean OA to at least 65.5% in these regions.



438



439 **Figure 9. The box-plot of the accuracy for twenty-one ecoregion zones. (a) overall accuracy, (b)kappa**  
 440 **coefficient. Ecoregion abbreviation and corresponding ecoregion is described in Table S2.**

441 **4.3.2 Inter-comparison based on the global patch-based samples**

442 Although the global point-based samples are adequate and even across the globe, the distribution of  
 443 points in each  $4^\circ \times 4^\circ$  geographical grid is too sparse to reflect the actual spatial pattern of the landscape.  
 444 Focusing on LC pattern at the local scale, we also used the global patch-based samples which can provide  
 445 spatial context information to conduct the accuracy assessment of the GLC-2015 map and compare  
 446 difference GLC products. Table 6 lists the accuracies of the GLC-2015 map and the other three GLC  
 447 products. Obviously, the GLC-2015 map achieved the best OA and kappa coefficient among these four  
 448 GLC maps. The accuracy gap between the GLC-2015 product and others was 5.6%-20.7%, which  
 449 presented a more significant variation compared with the result based on the global point-based samples.  
 450 In terms of PA and UA, the GLC-2015 map was higher than the other three ones in most LC classes, such  
 451 as forest, cropland, shrubland, and water bodies. Specifically, all the products had low accuracy for  
 452 grassland, shrubland, and wetland, similar to that in the accuracy assessment based on the global point-  
 453 based samples. It is evident that the FROM\_GLC had the worst performance in grassland, shrubland,  
 454 and wetland (as low as 3.2% for UA), implying that the classification method of FROM\_GLC is not  
 455 reliable for these three LC classes.

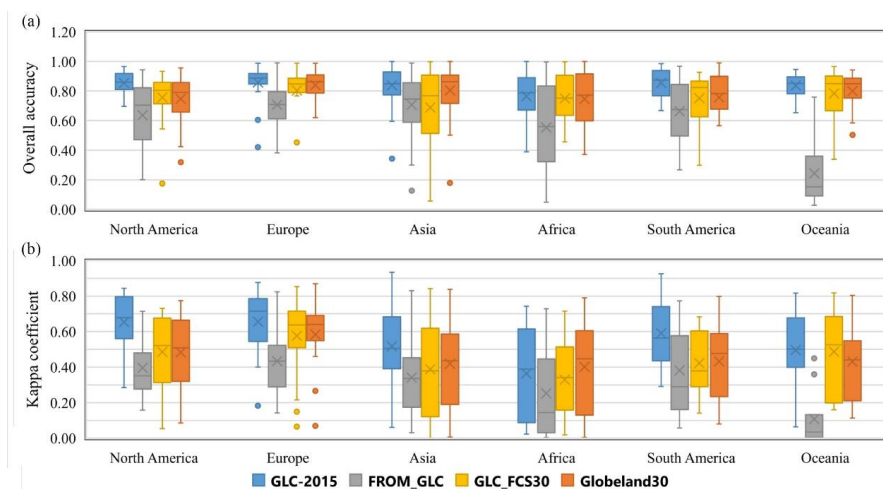
456 **Table 6. Mapping accuracy of the GLC-2015 map with the global patch-based samples**

		Cropland	Forest	Grassland	Shrubland	Wetland	Water bodies	Tundra	Impervious surfaces	Bare land	Permanent snow and ice	OA (Kappa coefficient)
GLC-2015	PA	0.862	0.899	0.622	0.565	0.234	0.944	0.683	0.740	0.747	0.820	0.838
	UA	0.918	0.811	0.633	0.673	0.647	0.916	0.881	0.719	0.604	0.750	(0.548)
Globeland30	PA	0.896	0.703	0.768	0.555	0.456	0.837	0.723	0.638	0.498	0.831	0.782
	UA	0.892	0.906	0.453	0.530	0.160	0.891	0.489	0.701	0.826	0.706	(0.437)
FROM_GLC	PA	0.483	0.714	0.633	0.221	0.032	0.912	0.761	0.504	0.672	0.501	0.631
	UA	0.873	0.804	0.189	0.119	0.187	0.883	0.714	0.804	0.482	0.703	(0.325)
GLC_FCS30	PA	0.865	0.780	0.395	0.563	0.364	0.878	0.058	0.643	0.644	0.742	0.742
	UA	0.860	0.831	0.510	0.332	0.135	0.941	0.575	0.639	0.459	0.752	(0.428)

457 Accuracy assessment was calculated in each patch-based sample, and box plots were produced for



458 each GLC product at the continental scale, as shown in Fig. 10. The GLC-2015 map showed a robust  
459 performance in each continent, with the highest accuracy among all the maps. Also, in all continents, the  
460 GLC-2015 map had the shortest boxes in terms of OA, which denoted that it had a more minor variation  
461 in accuracy at the continental scale. Among four products, the GLC\_FCS30 and Globeland30 achieved  
462 similar accuracies in most regions. Obviously, the FROM\_GLC gave the worst performance across  
463 different continents, especially in Oceania, where the OA for the FROM\_GLC was below 40.0%, namely  
464 most of the pixels in Oceania were incorrectly classified. We further compared mapping accuracies for  
465 each LC class in different continents (Fig. S1-S2). Since tundra and permanent snow and ice are rare and  
466 only existent in certain regions, they were not included in the comparison. As for PA across different  
467 continents, the GLC-2015 map outperformed other maps in cropland, forest, water bodies, impervious  
468 surfaces, and bare land. As for UA across different continents, the GLC-2015 map outperformed other  
469 maps in cropland, grassland, shrubland, wetland, impervious surfaces, and bare land, and achieved  
470 similar accuracies with the GLC\_FCS30 and Globeland30 in forest. Overall, the GLC-2015 map  
471 outperformed others regarding mapping accuracy at continental scale. In addition, all GLC products  
472 showed significant variation and low mean accuracy in grassland, shrubland, and wetland over most  
473 continents, which indicated that the mapping results for these three classes were not reliable enough.



474

475 **Figure 10. The box-plot of the accuracy for different continents, (a) overall accuracy, (b) kappa coefficient.**

476

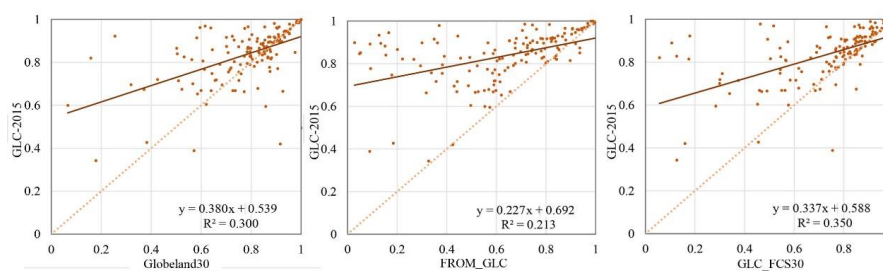
477

Furthermore, to compare the OA of the GLC-2015 map with other GLC products, scatter plots were used to describe the relationship between the overall accuracy of the GLC-2015 map and one other





478 product in each patch-based sample, as displayed in Fig. 11. Most of the points were above the 1:1 line,  
479 implying that the GLC-2015 map surpassed other GLC products in terms of OA. The distribution of  
480 points was more dispersed from the 1:1 line in the plot of the GLC-2015 map against FROM\_GLC  
481 compared to other plots. It indicated that these two products had a more significant difference, which  
482 was also proved in Table 6.



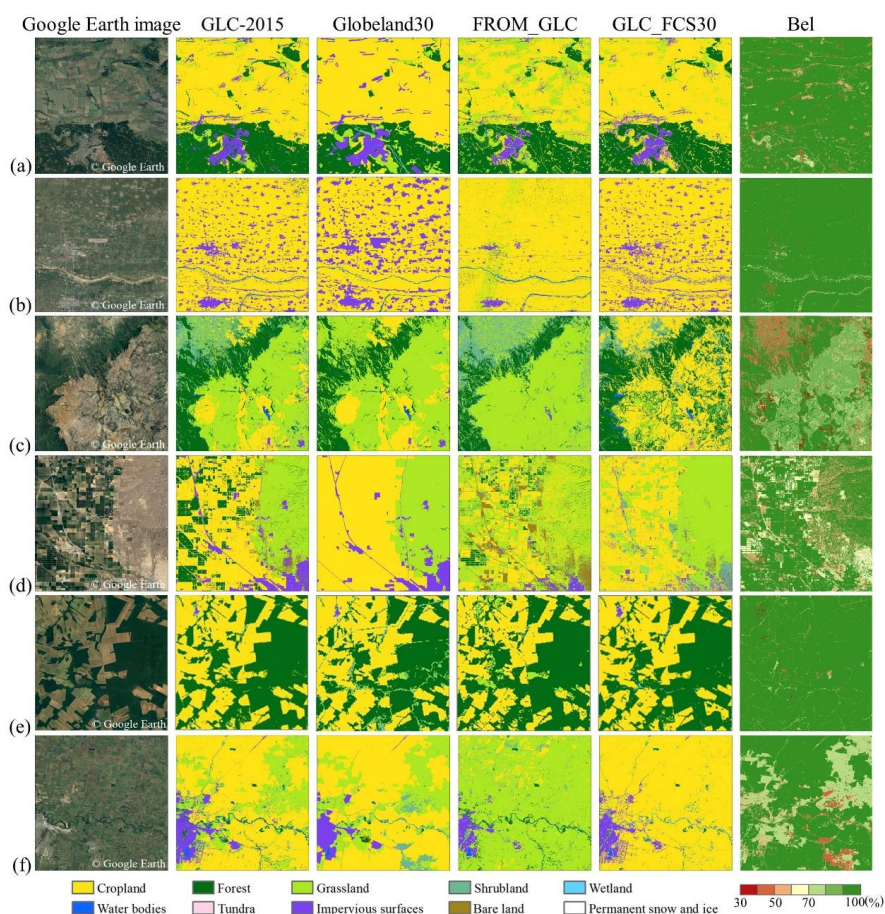
483  
484 **Figure 11. Scatter plots between the GLC-2015 map and other products obtained using the global patch-based**  
485 **samples.**

#### 486 4.3.3 Visual inter-comparison at the local scale

487 Except for quantitative accuracy assessment, we selected six typical geographical tiles covering six  
488 continents and different landscape environments to further present the mapping performance of the GLC-  
489 2015 map, Globeland30, FROM\_GLC, and GLC\_FCS30, as shown in Fig. 12. Overall, from a local  
490 point of view, the GLC-2015 map tended to be more diverse in LC classes and had better identification  
491 performance in various classes. In flattened cropland areas (Fig. 12a and Fig. 12b), the GLC-2015 map  
492 revealed diverse LC classes and accurately distinguished impervious surfaces; however, the Globeland30  
493 exaggerated the extent of impervious surfaces, and the remaining products failed to delineate impervious  
494 surfaces with small size. In addition, the FROM\_GLC misclassified some cropland pixels as grassland  
495 (Fig. 12a) and had an abnormal “stamp” (Fig. 12b). As for mountain areas (Fig. 12c and Fig. 12d), the  
496 GLC-2015 map uncovered the spatial pattern of natural and planted forest, cropland, and grassland. There  
497 were large confusions between cropland and grassland in the results of the FROM\_GLC and  
498 GLC\_FCS30, and some impervious surfaces and cropland areas were wrongly labeled as bare land by  
499 the FROM\_GLC. The areas (Fig. 12c), which were classified as forest, were misidentified as cropland  
500 and grassland in three other products. For the rainforest areas where a large number of trees were  
501 reclaimed for cropland (Fig. 12e), the GLC-2015 map, Globeland30, and GLC\_FCS30 had similarities  
502 in cropland areas; but the FROM\_GLC recognized some reclaimed areas as grassland. Additionally, the



503 GLC-2015 map accurately presented the spatial distribution of impervious surfaces while other products  
 504 had omission or commission errors. In the cropland-dominated areas (Fig. 12f), the GLC-2015 map and  
 505 Globeland30 showed a higher agreement, and both of them mapped the undulating areas as grassland.  
 506 Unlike the aforementioned two products, the FROM\_GLC misclassified large tracts of croplands as  
 507 grasslands, and the GLC\_FCS30 did not capture the grassland in undulating areas. Figure 12 also shows  
 508 the belief measure of the fused result in different geographical tiles. Although it does not directly evaluate  
 509 the mapping accuracy, it serves as a degree of support for the hypothesis of an accepted LC class being  
 510 true, it can still reflect the quality of the GLC-2015 map. Overall, Bel of the GLC-2015 map exceeded  
 511 80% in most areas of each tile, demonstrating the credibility and high quality of our mapping result.



512

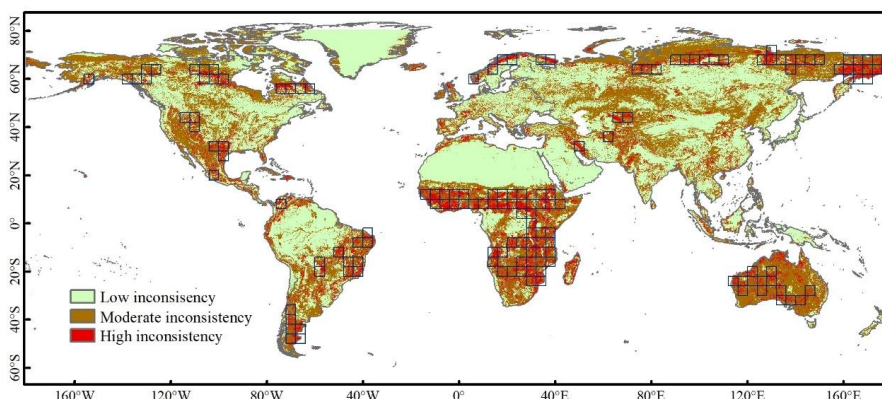
513 **Figure 12. Visual comparison between the GLC-2015 map and three other products for different continents.**

514 (a) to (f) are examples for Europe, Asia, Africa, North America, South America, and Oceania, respectively.



515 **4.4 Improvement of the GLC-2015 map**

516 The spatial distribution of consistency between three GLC products at the global scale is illustrated in  
517 Fig. 13. From the consistency map, we found that areas of low inconsistency mainly corresponded to  
518 homogeneous regions with simple LC classes. For example, the northern part of Africa was mainly  
519 classified as bare land, the northern part of South America was mainly classified as forest, and the  
520 Greenland was classified as permanent snow and ice. On the contrary, areas of high inconsistency were  
521 located in regions with complicated LC classes, especially in mixed vegetation regions or sparse  
522 vegetation regions, such as northern Asia, South Africa, Sahel region, Australia, northern and southern  
523 North America, and eastern and southern South America.



524 **Figure 13. Distribution of consistency between the Globeland30, FROM\_GLC, and GLC\_FCS30. The blue**  
525 **rectangles are high-inconsistency grids that the area of pixels with value equal to 1 account for more than 20%**  
526 **of the total area.**  
527

528 Based on the global point-based samples, we assessed the accuracies of the GLC-2015 map,  
529 Globeland30, FROM\_GLC, and GLC\_FCS30, in the aforementioned areas of low inconsistency,  
530 moderate inconsistency, and high inconsistency, as shown in Table 7. Overall, the GLC-2015 map had  
531 the highest accuracies against the other three ones in three areas. For each product, areas of low  
532 inconsistency obtained the highest accuracies, followed by areas of moderate inconsistency and then high  
533 inconsistency, which demonstrated that inconsistency of the existing products could indicate the quality  
534 of maps. In areas of low inconsistency, the overall accuracy gap between the GLC-2015 map and  
535 previous ones was as small as 0.2%-1%. However, for areas of moderate and high inconsistency, the  
536 comparison accuracy gap expanded to 17.6%-23.2% and 21.0%-25.2%, respectively. It proved the  
537 overwhelming superiority of the GLC-2015 map over the other three products in the areas of high

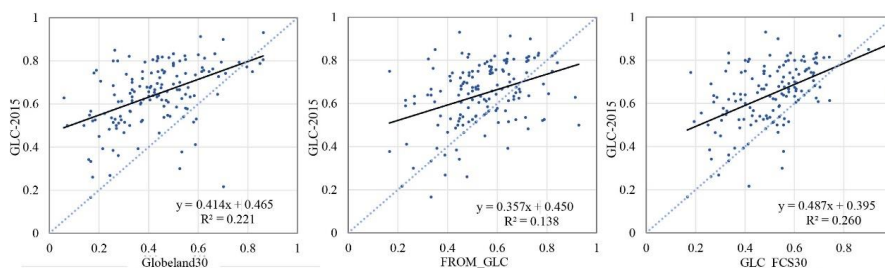


538 identification difficulty.

539 **Table 7. Accuracy assessments of the GLC products in three areas.**

	GLC-2015		Globeland30		FROM_GLC		GLC_FCS30	
	OA	Kappa	OA	Kappa	OA	Kappa	OA	Kappa
Areas of low inconsistency	0.939	0.922	0.931	0.912	0.929	0.909	0.937	0.919
Areas of moderate inconsistency	0.717	0.671	0.534	0.467	0.485	0.416	0.541	0.464
Areas of high inconsistency	0.509	0.430	0.285	0.196	0.299	0.212	0.257	0.144

540 We further provided a comparative analysis of three previous GLC products and the GLC-2015 map  
 541 in areas of high inconsistency. We calculated the area of pixels with a value equal to 1 in  $4^\circ \times 4^\circ$  grids.  
 542 The grids that the area of pixels with a value equal to 1 account for more than 20% of the total area was  
 543 selected as grids of high inconsistency. Finally, a total number of 147 grids were selected (Fig. 13). To  
 544 compare the accuracy of the GLC-2015 map and other ones, we utilized scatter plots to represent the  
 545 relationship between the overall accuracy of one previous product and the GLC-2015 map in each grid  
 546 of high inconsistency based on the global point-based samples (Fig. 14). Most of the points were above  
 547 the 1:1 line, namely the values of y-axes corresponding to those points were larger than the values of x-  
 548 axes, which demonstrated that the GLC-2015 map performed better than other GLC products in most  
 549 grids of high inconsistency. It can be found that the fitting line in each scatter plot had the intercept  
 550 exceeding 0.39, the slope less than 0.50, and the  $R^2$  less than 0.30, showing that the GLC-2015 map had  
 551 a large difference with other ones.

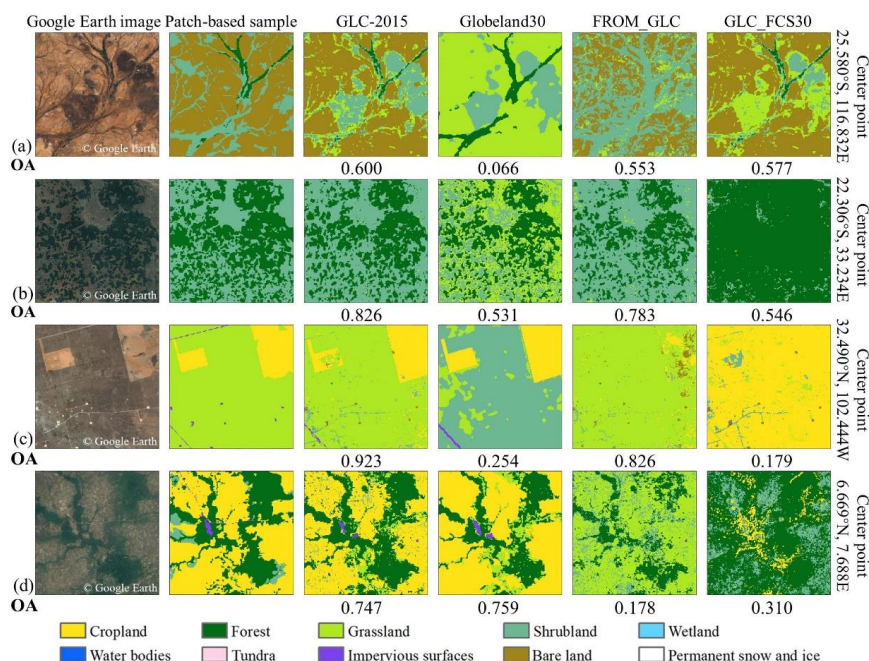


552  
 553 **Figure 14. Overall accuracy relationship between the GLC-2015 map and other products in grids of high**  
 554 **inconsistency.**

555 To intuitively compare the mapping result of the GLC-2015 map and three existing ones in areas of  
 556 high inconsistency, we focused on visual inspection in various areas based on four  $5\text{ km} \times 5\text{ km}$  patch-



557 based samples and conducted accuracy statistics, as shown in Fig 15. In the detailed display, it is apparent  
558 that three previous products had a large difference in four areas. As can be seen from the four visual cases,  
559 the typical confusions between LC classes in areas of high inconsistency were as follows: (1) shrubland  
560 was easily misclassified as forest and grassland; (2) cropland, grassland, and shrubland were heavily  
561 confused with each other; (3) bare land was likely to be mixed with shrubland and grassland. Except for  
562 Fig.14d, the GLC-2015 map surpassed other products in the local accuracy assessment. In Western  
563 Australian mulga shrublands (Fig. 15a), the GLC-2015 map and GLC\_FCS30 showed similar spatial  
564 distribution and shape of bare land and forest, which was consistent with the real landscape. While the  
565 Globeland30 wrongly classified bare land as grassland and the FROM\_GLC under-classified bare land.  
566 As for Zambebian and mopane woodlands (Fig. 15b), the GLC-2015 map performed best with OA  
567 reaching 82.6%, followed by the FROM\_GLC. In contrast, other products failed to distinguish shrubland  
568 from forest. In Western short grasslands (Fig. 15c), the GLC-2015 map had a similar mapping result with  
569 the ground truth, with only slight differences in detail. In the results of the Globeland30 and GLC\_FCS30,  
570 grassland was poorly classified. When it comes to Guinean forest-savanna mosaic (Fig. 15d), the GLC-  
571 2015 map and Globeland30 showed high spatial consistency, and both had accurate classification profile  
572 for cropland, forest, and impervious surfaces, while other products misidentified cropland as other LC  
573 classes.



574

575 **Figure 15. Visual comparison between the GLC-2015 map and three other products based on 5km × 5km**  
 576 **patch-based samples and Google Earth images for four areas of high inconsistency (a-d). The OA for each**  
 577 **product was calculated by the corresponding patch-based sample.**

578 **5. Data availability**

579 The improved global land cover map in 2015 with 30 m resolution is available at  
 580 <https://doi.org/10.6084/m9.figshare.19752856.v1> (Li et al., 2022). The GLC-2015 product is organized  
 581 by a total of 1507 4° × 4° geographical grids in GeoTIFF format across the world's terrestrial area. Each  
 582 image of the GLC-2015 product is named as "GLC-2015\_i" (i represents the id of the 4-degree grid).

583 **6. Conclusions**

584 GLC information at fine spatial resolution is vital for the global environment and climate studies which  
 585 can capture most human activity. Resulting from the differences in classification scheme, satellite sensor  
 586 data, classification algorithms and sampling strategies, the existing GLC products have high  
 587 inconsistency in some parts of the world, especially in fragmented areas and transition zones. More  
 588 accurate and reliable data with accuracy improved in areas of high mapping inconsistency is very



589 desirable. In this study, with the help of the GEE platform, we developed the GLC-2015 map by  
590 integrating multiple existing GLC maps based on the DSET. The GLC-2015 map can significantly  
591 increase the mapping accuracy and possess good recognition performance in various LC classes.

592 The GLC-2015 map was validated by both the global point-based samples and the global patch-  
593 based samples. Accuracy assessments show that the GLC-2015 map achieved an OA of 76.0%, a kappa  
594 coefficient of 0.715 using a total of 34,987 global point-based samples, and an OA of 83.8%, a kappa  
595 coefficient of 0.548 using a total of 144 global patch-based samples. Data inter-comparison indicated  
596 that the GLC-2015 map surpassed other three products both visually and quantitatively, by OA  
597 improvement of 12.5%-14.7% validated with the global point-based samples and 5.6%-20.7% with the  
598 global patch-based samples. Compared to other products, there are fewer misclassifications in the GLC-  
599 2015 map for most LC classes, such as forest, cropland, shrubland, and water bodies. Meanwhile, the  
600 GLC-2015 map outperformed others in terms of OA and kappa coefficient across different ecoregions  
601 and different continents. Notably, the GLC-2015 map showed great superiority over others by an  
602 increment of 0.2%-1.0% in overall accuracy for areas of low inconsistency, 17.6%-23.2% for areas of  
603 moderate inconsistency, and 21.0%-25.2% for areas of high inconsistency. Therefore, it can be concluded  
604 that the GLC-2015 map is a robust and reliable map that can significantly improve mapping accuracy  
605 compared to previous GLC products.

#### 606 **Author contributions**

607 XL and XX conceived the research. BL and XU designed and carried out the experiments. QS and DH  
608 provided data. BL wrote the original manuscript. XX, HZ and YC reviewed the writing.

#### 609 **Competing interests**

610 The authors declare that they have no conflict of interest.

#### 611 **Financial support**

612 This research has been supported by the National Key Research & Development Program of China (Grant  
613 No. 2019YFA0607203), the National Natural Science Foundation of China (Grant No. 42001326,  
614 42171409), and the Natural Science Foundation of Guangdong Province of China (Grant No.



615 2022A1515012207).

## 616 **References**

- 617 Ban, Y., Gong, P., and Giri, C.: Global land cover mapping using Earth observation satellite data: Recent  
618 progresses and challenges, *ISPRS J. Photogramm. Remote Sens.*, 103, 1-6,  
619 <https://doi.org/10.1016/j.isprsjprs.2015.01.001>, 2015.
- 620 Bartholomé, E. and Belward, A. S.: GLC2000: A new approach to global land cover mapping from Earth  
621 observation data, *Int. J. Remote Sens.*, 26, 1959-1977, <https://doi.org/10.1080/01431160412331291297>,  
622 2005.
- 623 Bounoua, L., DeFries, R., Collatz, G. J., Sellers, P., and Khan, H.: Effects of land cover conversion on  
624 surface climate, *Climatic Change*, 52, 29-64, <https://doi.org/10.1023/A:1013051420309>, 2002.
- 625 Bunting, P., Rosenqvist, A., Lucas, R. M., Rebelo, L.-M., Hilarides, L., Thomas, N., Hardy, A., Itoh, T.,  
626 Shimada, M., and Finlayson, C. M.: The Global Mangrove Watch—A new 2010 global baseline of  
627 mangrove extent, *Remote Sens.*, 10, <https://doi.org/10.3390/rs10101669>, 2018.
- 628 Chapin, F. S. I., Zavaleta, E. S., Eviner, V. T., Naylor, R. L., Vitousek, P. M., Reynolds, H. L., Hooper,  
629 D. U., Lavorel, S., Sala, O. E., Hobbie, S. E., Mack, M. C., and Díaz, S.: Consequences of changing  
630 biodiversity, *Nature*, 405, 234-242, <https://doi.org/10.1038/35012241>, 2000.
- 631 Chen, J., Chen, J., Liao, A., Cao, X., Chen, L., Chen, X., He, C., Han, G., Peng, S., Lu, M., Zhang, W.,  
632 Tong, X., and Mills, J.: Global land cover mapping at 30m resolution: A POK-based operational approach,  
633 *ISPRS J. Photogramm. Remote Sens.*, 103, 7-27, <https://doi.org/10.1016/j.isprsjprs.2014.09.002>, 2015.
- 634 Clinton, N., Yu, L., and Gong, P.: Geographic stacking: Decision fusion to increase global land cover  
635 map accuracy, *ISPRS J. Photogramm. Remote Sens.*, 103, 57-65,  
636 <https://doi.org/10.1016/j.isprsjprs.2015.02.010>, 2015.
- 637 Land Cover CCI: Product User Guide Version 2: [https://www.esa-landcover-cci.org/?q=webfm\\_send/84](https://www.esa-landcover-cci.org/?q=webfm_send/84),  
638 last access: 21 January 2022.
- 639 DeFries, R. S., Houghton, R. A., Hansen, M. C., Field, C. B., Skole, D., and Townshend, J.: Carbon  
640 emissions from tropical deforestation and regrowth based on satellite observations for the 1980s and  
641 1990s, *Proc. Natl. Acad. Sci. U.S.A.*, 99, 14256, <https://doi.org/10.1073/pnas.182560099>, 2002.
- 642 Foley, J. A., DeFries, R., Asner, G. P., Barford, C., Bonan, G., Carpenter, S. R., Chapin, F. S., Coe, M. T.,  
643 Daily, G. C., Gibbs, H. K., Helkowski, J. H., Holloway, T., Howard, E. A., Kucharik, C. J., Monfreda,  
644 C., Patz, J. A., Prentice, I. C., Ramankutty, N., and Snyder, P. K.: Global Consequences of Land Use,  
645 *Science*, 309, 570-574, <https://doi.org/10.1126/science.1111772>, 2005.
- 646 Friedl, M. A., Sulla-Menashe, D., Tan, B., Schneider, A., Ramankutty, N., Sibley, A., and Huang, X.:  
647 MODIS Collection 5 global land cover: Algorithm refinements and characterization of new datasets,  
648 *Remote Sens. Environ.*, 114, 168-182, <https://doi.org/10.1016/j.rse.2009.08.016>, 2010.
- 649 Fritz, S., You, L., Bun, A., See, L., McCallum, I., Schill, C., Perger, C., Liu, J., Hansen, M., and  
650 Obersteiner, M.: Cropland for sub-Saharan Africa: A synergistic approach using five land cover data sets,  
651 *Geophys. Res. Lett.*, 38, L04404, <https://doi.org/10.1029/2010GL046213>, 2011.
- 652 Gao, Y., Liu, L., Zhang, X., Chen, X., Mi, J., and Xie, S.: Consistency Analysis and Accuracy Assessment  
653 of Three Global 30-m Land-Cover Products over the European Union using the LUCAS Dataset, *Remote  
654 Sens.*, 12, 3479, <https://doi.org/10.3390/rs12213479>, 2020.
- 655 Giri, C., Zhu, Z., and Reed, B.: A comparative analysis of the Global Land Cover 2000 and MODIS land





- 656 cover data sets, *Remote Sens. Environ.*, 94, 123-132, <https://doi.org/10.1016/j.rse.2004.09.005>, 2005.
- 657 Giri, C., Pengra, B., Long, J., and Loveland, T. R.: Next generation of global land cover characterization,  
658 mapping, and monitoring, *Int. J. Appl. Earth Obs. Geoinf.*, 25, 30-37,  
659 <https://doi.org/10.1016/j.jag.2013.03.005>, 2013.
- 660 Gómez, C., White, J. C., and Wulder, M. A.: Optical remotely sensed time series data for land cover  
661 classification: A review, *ISPRS J. Photogramm. Remote Sens.*, 116, 55-72,  
662 <https://doi.org/10.1016/j.isprsjprs.2016.03.008>, 2016.
- 663 Gong, P.: Remote sensing of environmental change over China: A review, *Sci. Bull.*, 57, 2793-2801,  
664 <https://doi.org/10.1007/s11434-012-5268-y>, 2012.
- 665 Gong, P., Yu, L., Li, C., Wang, J., Liang, L., Li, X., Ji, L., Bai, Y., Cheng, Y., and Zhu, Z.: A new research  
666 paradigm for global land cover mapping, *Ann. GIS*, 22, 87-102,  
667 <https://doi.org/10.1080/19475683.2016.1164247>, 2016.
- 668 Gong, P., Wang, J., Yu, L., Zhao, Y., Zhao, Y., Liang, L., Niu, Z., Huang, X., Fu, H., Liu, S., Li, C., Li,  
669 X., Fu, W., Liu, C., Xu, Y., Wang, X., Cheng, Q., Hu, L., Yao, W., Zhang, H., Zhu, P., Zhao, Z., Zhang,  
670 H., Zheng, Y., Ji, L., Zhang, Y., Chen, H., Yan, A., Guo, J., Yu, L., Wang, L., Liu, X., Shi, T., Zhu, M.,  
671 Chen, Y., Yang, G., Tang, P., Xu, B., Giri, C., Clinton, N., Zhu, Z., Chen, J., and Chen, J.: Finer resolution  
672 observation and monitoring of global land cover: first mapping results with Landsat TM and ETM+ data,  
673 *Int. J. Remote Sens.*, 34, 2607-2654, <https://doi.org/10.1080/01431161.2012.748992>, 2013.
- 674 Grekousis, G., Mountrakis, G., and Kavouras, M.: An overview of 21 global and 43 regional land-cover  
675 mapping products, *Int. J. Remote Sens.*, 36, 5309-5335, <https://doi.org/10.1080/01431161.2015.1093195>,  
676 2015.
- 677 Grimm, N. B., Faeth, S. H., Golubiewski, N. E., Redman, C. L., Wu, J., Bai, X., and Briggs, J. M.: Global  
678 change and the ecology of cities, *Science*, 319, 756-760, <https://doi.org/10.1126/science.1150195>, 2008.
- 679 Hansen, M. C., Defries, R. S., Townshend, J. R. G., and Sohlberg, R.: Global land cover classification at  
680 1 km spatial resolution using a classification tree approach, *Int. J. Remote Sens.*, 21, 1331-1364,  
681 <https://doi.org/10.1080/014311600210209>, 2000.
- 682 Hansen, M. C., Potapov, P. V., Moore, R., Hancher, M., Turubanova, S. A., Tyukavina, A., Thau, D.,  
683 Stehman, S. V., Goetz, S. J., Loveland, T. R., Kommareddy, A., Egorov, A., Chini, L., Justice, C. O., and  
684 Townshend, J. R. G.: High-resolution global maps of 21st-century forest cover change, *Science*, 342,  
685 850-853, <https://doi.org/10.1126/science.1244693>, 2013.
- 686 Herold, M., Mayaux, P., Woodcock, C. E., Baccini, A., and Schmullius, C.: Some challenges in global  
687 land cover mapping: An assessment of agreement and accuracy in existing 1 km datasets, *Remote Sens.*  
688 *Environ.*, 112, 2538-2556, <https://doi.org/10.1016/j.rse.2007.11.013>, 2008.
- 689 Jung, M., Henkel, K., Herold, M., and Churkina, G.: Exploiting synergies of global land cover products  
690 for carbon cycle modeling, *Remote Sens. Environ.*, 101, 534-553,  
691 <https://doi.org/10.1016/j.rse.2006.01.020>, 2006.
- 692 Kang, J., Wang, Z., Sui, L., Yang, X., Ma, Y., and Wang, J.: Consistency Analysis of Remote Sensing  
693 Land Cover Products in the Tropical Rainforest Climate Region: A Case Study of Indonesia, *Remote*  
694 *Sen.*, 12, 1410, <https://doi.org/10.3390/rs12091410>, 2020.
- 695 Li, B., Xu, X., Liu, X., Shi, Q., Zhuang, H., Cai, Y., and He, D.: An improved global land cover mapping  
696 in 2015 with 30 m resolution (GLC-2015) based on a multi-source product fusion approach, *Figshare*,  
697 <https://doi.org/10.6084/m9.figshare.19752856.v1>, 2022.
- 698 Li, C., Gong, P., Wang, J., Zhu, Z., Biging, G. S., Yuan, C., Hu, T., Zhang, H., Wang, Q., Li, X., Liu, X.,  
699 Xu, Y., Guo, J., Liu, C., Hackman, K. O., Zhang, M., Cheng, Y., Yu, L., Yang, J., Huang, H., and Clinton,



- 700 N.: The first all-season sample set for mapping global land cover with Landsat-8 data, *Sci. Bull.*, 62, 508-  
701 515, <https://doi.org/10.1016/j.scib.2017.03.011>, 2017.
- 702 Liu, H., Gong, P., Wang, J., Clinton, N., Bai, Y., and Liang, S.: Annual dynamics of global land cover  
703 and its long-term changes from 1982 to 2015, *Earth Syst. Sci. Data*, 12, 1217-1243,  
704 <https://doi.org/10.5194/essd-12-1217-2020>, 2020a.
- 705 Liu, H., Gong, P., Wang, J., Wang, X., Ning, G., and Xu, B.: Production of global daily seamless data  
706 cubes and quantification of global land cover change from 1985 to 2020 - iMap World 1.0, *Remote Sens.*  
707 *Environ.*, 258, 112364, <https://doi.org/10.1016/j.rse.2021.112364>, 2021a.
- 708 Liu, L., Zhang, X., Gao, Y., Chen, X., Shuai, X., and Mi, J.: Finer-resolution mapping of global land  
709 cover: Recent developments, consistency analysis, and prospects, *Journal of Remote Sensing*, 2021,  
710 5289697, <https://doi.org/10.34133/2021/5289697>, 2021b.
- 711 Liu, X., Huang, Y., Xu, X., Li, X., Li, X., Ciais, P., Lin, P., Gong, K., Ziegler, A. D., Chen, A., Gong, P.,  
712 Chen, J., Hu, G., Chen, Y., Wang, S., Wu, Q., Huang, K., Estes, L., and Zeng, Z.: High-spatiotemporal-  
713 resolution mapping of global urban change from 1985 to 2015, *Nature Sustainability*, 3, 564-570,  
714 <https://doi.org/10.1038/s41893-020-0521-x>, 2020b.
- 715 Loveland, T. R., Reed, B. C., Brown, J. F., Ohlen, D. O., Zhu, Z., Yang, L., and Merchant, J. W.:  
716 Development of a global land cover characteristics database and IGBP DISCover from 1 km AVHRR  
717 data, *Int. J. Remote Sens.*, 21, 1303-1330, <https://doi.org/10.1080/014311600210191>, 2000.
- 718 Ludwig, C., Walli, A., Schleicher, C., Weichselbaum, J., and Riffler, M.: A highly automated algorithm  
719 for wetland detection using multi-temporal optical satellite data, *Remote Sens. Environ.*, 224, 333-351,  
720 <https://doi.org/10.1016/j.rse.2019.01.017>, 2019.
- 721 Mayaux, P., Bartholomé, E., Fritz, S., and Belward, A.: A New Land-Cover Map of Africa for the Year  
722 2000, *J. Biogeogr.*, 31, 861-877, <https://doi.org/10.1111/j.1365-2699.2004.01073.x>, 2004.
- 723 Moody, A. and Woodcock, C.: Scale-dependent errors in the estimation of land-cover proportions:  
724 Implications for global land-cover datasets, *Photogramm. Eng. Rem. S.*, 60, 585-594, 1994.
- 725 Pekel, J.-F., Cottam, A., Gorelick, N., and Belward, A. S.: High-resolution mapping of global surface  
726 water and its long-term changes, *Nature*, 540, 418-422, <https://doi.org/10.1038/nature20584>, 2016.
- 727 Rottensteiner, F., Trinder, J. C., Clode, S., and Kubik, K.: Using the Dempster-Shafer method for the  
728 fusion of LIDAR data and multi-spectral images for building detection, *Inform. Fusion.*, 6, 283-300,  
729 <https://doi.org/10.1016/j.inffus.2004.06.004>, 2005.
- 730 Running, S. W.: Ecosystem disturbance, carbon, and climate, *Science*, 321, 652-653,  
731 <https://doi.org/10.1126/science.1159607>, 2008.
- 732 Schewe, J., Gosling, S. N., Reyer, C., Zhao, F., Ciais, P., Elliott, J., Francois, L., Huber, V., Lotze, H. K.,  
733 Seneviratne, S. I., van Vliet, M. T. H., Vautard, R., Wada, Y., Breuer, L., Büchner, M., Carozza, D. A.,  
734 Chang, J., Coll, M., Deryng, D., de Wit, A., Eddy, T. D., Folberth, C., Frieler, K., Friend, A. D., Gerten,  
735 D., Gudmundsson, L., Hanasaki, N., Ito, A., Khabarov, N., Kim, H., Lawrence, P., Morfopoulos, C.,  
736 Müller, C., Müller Schmied, H., Orth, R., Ostberg, S., Pokhrel, Y., Pugh, T. A. M., Sakurai, G., Satoh, Y.,  
737 Schmid, E., Stacke, T., Steenbeek, J., Steinkamp, J., Tang, Q., Tian, H., Tittensor, D. P., Volkholz, J.,  
738 Wang, X., and Warszawski, L.: State-of-the-art global models underestimate impacts from climate  
739 extremes, *Nat. Commun.*, 10, 1005, <https://doi.org/10.1038/s41467-019-08745-6>, 2019.
- 740 See, L., Schepaschenko, D., Lesiv, M., McCallum, I., Fritz, S., Comber, A., Perger, C., Schill, C., Zhao,  
741 Y., Maus, V., Siraj, M. A., Albrecht, F., Cipriani, A., Vakolyuk, M. y., Garcia, A., Rabia, A. H., Singha,  
742 K., Marcarini, A. A., Kattenborn, T., Hazarika, R., Schepaschenko, M., van der Velde, M., Kraxner, F.,  
743 and Obersteiner, M.: Building a hybrid land cover map with crowdsourcing and geographically weighted



- 744 regression, *ISPRS J. Photogramm. Remote Sens.*, 103, 48-56,  
745 <https://doi.org/10.1016/j.isprsjprs.2014.06.016>, 2015.
- 746 Song, X.-P., Huang, C., and Townshend, J. R.: Improving global land cover characterization through data  
747 fusion, *Geo-Spat. Inf. Sci.*, 20, 141-150, <https://doi.org/10.1080/10095020.2017.1323522>, 2017.
- 748 Song, X.-P., Hansen, M. C., Stehman, S. V., Potapov, P. V., Tyukavina, A., Vermote, E. F., and Townshend,  
749 J. R.: Global land change from 1982 to 2016, *Nature*, 560, 639-643, <https://doi.org/10.1038/s41586-018-0411-9>, 2018.
- 750
- 751 Sun, B., Chen, X., and Zhou, Q.: Uncertainty assessment of GlobeLand30 land cover data set over central  
752 Asia, *Int. Arch. Photogramm. Remote Sens. Spat. Inf. Sci.*, 41, 1313, <https://doi.org/10.5194/isprs-archives-XLI-B8-1313-2016>, 2016.
- 753
- 754 Verburg, P. H., Neumann, K., and Nol, L.: Challenges in using land use and land cover data for global  
755 change studies, *Glob. Change Biol.*, 17, 974-989, <https://doi.org/10.1111/j.1365-2486.2010.02307.x>,  
756 2011.
- 757 Verburg, P. H., Mertz, O., Erb, K.-H., Haberl, H., and Wu, W.: Land system change and food security:  
758 towards multi-scale land system solutions, *Curr. Opin. Environ. Sustain.*, 5, 494-502,  
759 <https://doi.org/10.1016/j.cosust.2013.07.003>, 2013.
- 760 Yang, J. and Huang, X.: The 30 m annual land cover dataset and its dynamics in China from 1990 to  
761 2019, *Earth Syst. Sci. Data*, 13, 3907-3925, <https://doi.org/10.5194/essd-13-3907-2021>, 2021.
- 762 Yang, J., Gong, P., Fu, R., Zhang, M., Chen, J., Liang, S., Xu, B., Shi, J., and Dickinson, R.: The role of  
763 satellite remote sensing in climate change studies, *Nat. Clim. Chang.*, 3, 875-883,  
764 <https://doi.org/10.1038/nclimate1908>, 2013.
- 765 Yang, Y., Xiao, P., Feng, X., and Li, H.: Accuracy assessment of seven global land cover datasets over  
766 China, *ISPRS J. Photogramm. Remote Sens.*, 125, 156-173,  
767 <https://doi.org/10.1016/j.isprsjprs.2017.01.016>, 2017.
- 768 Zhang, C., Dong, J., and Ge, Q.: Quantifying the accuracies of six 30-m cropland datasets over China: A  
769 comparison and evaluation analysis, *Comput. Electron. Agric.*, 197, 106946,  
770 <https://doi.org/10.1016/j.compag.2022.106946>, 2022.
- 771 Zhang, X., Liu, L., Chen, X., Gao, Y., Xie, S., and Mi, J.: GLC\_FCS30: global land-cover product with  
772 fine classification system at 30 m using time-series Landsat imagery, *Earth Syst. Sci. Data*, 13, 2753-  
773 2776, <https://doi.org/10.5194/essd-13-2753-2021>, 2021.
- 774